ACS APPLIED MATERIALS & INTERFACES

Article

Investigating Water Splitting with CaFe2O4 Photocathodes by Electrochemical Impedance Spectroscopy

María Isabel Díez-García, and Roberto Gómez

ACS Appl. Mater. Interfaces, **Just Accepted Manuscript** • DOI: 10.1021/acsami.6b07465 • Publication Date (Web): 28 Jul 2016

ACS Publications

ACS Applied Materials & Interfaces is published by the American Chemical Society.
1155 Sixteenth Street N.W., Washington, DC 20036

Investigating Water Splitting with $CaFe_2O_4$ Photocathodes by Electrochemical Impedance Spectroscopy

*María Isabel Díez-García, Roberto Gómez**

Departament de Química Física i Institut Universitari d'Electroquímica, Universitat d'Alacant, Apartat 99, E-03080 Alacant, Spain

KEYWORDS: $CaFe_2O_4$, p-type, oxide, photocathode, water splitting, hydrogen, electrochemical impedance spectroscopy, kinetic model

ABSTRACT

Artificial photosynthesis constitutes one of the most promising alternatives for harvesting solar energy in the form of fuels, such as hydrogen. Among the different devices that could be developed to achieve efficient water photosplitting, tandem photoelectrochemical cells show more flexibility and offer high theoretical conversion efficiency. The development of these cells depends on finding efficient and stable photoanodes and, particularly, photocathodes, which requires having reliable information on the mechanism of charge transfer at the semiconductor/solution interface. In this context, this work deals with the preparation of thin film calcium ferrite electrodes and their photoelectrochemical characterization for hydrogen generation by means of electrochemical impedance spectroscopy (EIS). A fully theoretical model that includes elementary steps for charge transfer to the electrolyte and surface recombination with photogenerated holes is presented. The model also takes into account the complexity of the semiconductor/solution interface by including the capacitances of the space charge region, the surface states and the Helmholtz layer (as a constant phase element). After illustrating the predicted Nyquist plots in a general manner, the experimental results for calcium ferrite electrodes at different applied potentials and under different illumination intensities are fitted to the model. The excellent agreement between the model and the experimental results is illustrated by the simultaneous fit of both the Nyquist and the Bode plots. The concordance between both theory and experiments allows us to conclude that a direct transfer of electrons from the conduction band to water prevails for hydrogen photogeneration on calcium ferrite electrodes and that most of the carrier recombination occurs in the material bulk. In more

general vein, this study illustrates how the use of EIS may provide important clues about the behavior of photoelectrodes and the main strategies for their improvement.

1. INTRODUCTION

The problem of maintaining the growing demand of energy has attracted considerable interest in our society. The imminent depletion of fossil fuels motivates research in energy clean and renewable energy generation. In this respect, water splitting has been presented as a relevant approach to produce hydrogen or other valuables fuels such as methanol using CO_2 as a precursor. Probably, the most practical device for water photosplitting is a tandem cell composed of an adequate couple of photocathode/photoanode that can decompose water into hydrogen and oxygen gases using only solar energy without the need of an applied bias.

TiO_2 used as a photoanode has reached high efficiencies although it only absorbs a small portion of the solar spectrum.[1–3] Acceptable efficiencies have also been obtained with other materials having lower band gaps such as hematite or $BiVO_4$.[4–8] Traditionally, the most studied photocathode oxide materials were based on copper, especially Cu_2O.[9–12] It is worth nothing that the reports dealing with photocathode materials are scarcer, mainly because in general p-type semiconductor metal oxides present a limited corrosion resistance and a low carrier mobility. Recently, many efforts have been focused on finding highly efficient and highly stable photocathodes. Ternary oxides have been presented as good candidates because many of them are able to absorb visible light and have suitable band edge positions for water reduction. Indeed, a number of ternary oxides such as $LaFeO_3$,[13,14] $CuCrO_2$,[15]

$CuFeO_2$,[16] or $CuNbO_3$,[17] have recently been studied as photocathodic materials. In addition, there are some earlier studies on $CaFe_2O_4$, $Sr_7Fe_{10}O_{22}$,[18] and $LuRhO_3$.[19]

As far as we know, $CaFe_2O_4$ is among the most studied ternary oxide photocathodes for water splitting. Having a relatively narrow band gap (1.9 eV), it is able to absorb visible light, and it also has a suitable band edge positions for water reduction. In addition, it can be prepared from cheap reagents. Its photoelectrochemical properties for hydrogen evolution were first described by Matsumoto et al.[18] Compared with other p-type metal oxides, relatively high efficiencies for water splitting have been reached by preparing this material as a compact film.[20,21] However, the efficiency is still low and the temperature necessary for electrode preparation is high, which are the main drawbacks for its practical use. Nowadays, finding a cost-effective method for $CaFe_2O_4$ electrode preparation is still a challenge.

It is important to highlight that the knowledge of the different processes and reactions that take place in the photoactive material is critical for the improvement of the photoelectrochemical performance of the electrodes. Not only the semiconductor/electrolyte interface (SEI) plays a key role, but also the characteristics of the material bulk, where recombination processes may take place. Non-stationary photoelectrochemical impedance spectroscopy is a powerful in situ technique for the understanding of the processes at illuminated SEIs. It can provide useful information about the kinetics of the different steps and the nature of the chemical capacitance. For instance, it could help identify the rate determining step of the charge transfer reaction. The most common approach to analyze the electrochemical impedance spectroscopy (EIS) results is based upon an equivalent circuit of capacitors and resistances representing the SEI.[22–27]

This strategy leads to a good fit of the experimental values, and provides information about resistive and capacitive elements related with the phenomena occurring at the SEI, but it has the disadvantage that some of the elements of the circuits have an unclear physical meaning, especially those related with the kinetics and reaction mechanisms involving the charge carriers.

In this paper, not only the chemical capacitance in the SEI, but also the kinetics of the hydrogen evolution photoelectrochemical reaction for a p-type $CaFe_2O_4$ electrode is analyzed by means of EIS. We have developed a model on the basis of the work of Leng et al,[28] which was focused on the kinetics of a photooxidation reaction on TiO_2 electrodes, but adapted to H_2 evolution over p-type photoelectrodes. The importance of both defining the characteristics of the interface employed to build the mathematical model, and establishing convenient approximations in view of extracting electrochemical information from the experimental analysis are highlighted.

2. THEORETICAL BASIS

2.1. Mechanism and theoretical approach

The photoelectrochemical interpretation of EIS experiments using kinetic models instead of equivalent circuits has been mainly developed for n-type semiconductors.[28–30] Generally, the resulting equations are also valid for p-type electrodes with the appropriate current sign reversal. For instance, Ponomarev and Peter[31] investigated recombination, charge transfer rate constants, and space charge capacitance for a p-type InP electrode. However, to the best of our knowledge, the present work is the first in investigating the water reduction

process in a p-type metal oxide electrode on the basis of a kinetic model for EIS. The general description of the proposed model derives from the analysis performed by Leng et al,[28] considering not only the transfer of electrons to the electrolyte from the conduction band, but also from surface states, as well as the recombination of electron-holes pairs in the bulk and/or at surface states.

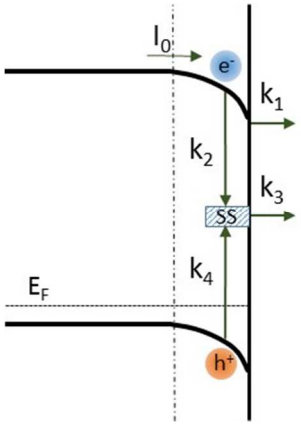

Figure 1. Scheme showing the different processes of charge transfer at the p-type/electrolyte interface under illumination.

As shown in figure 1, the mechanism considers surface states situated at a certain energy above the Fermi level of the semiconductor. The mechanisms that govern the water reduction process can be represented by the following kinetic reactions:

$$SC + h\upsilon \rightarrow h_{VB} + e_{CB} \quad (0)$$

$$v_0 = I_0$$

$$e_{CB} + H_2O \xrightarrow{k_1'} H_{ads} + OH^- \quad (1)$$

$$v_1 = k_1'[H_2O]n_1 = k_1 n_1$$

$$e_{CB} + SS^0 \xrightarrow{k_2'} SS^- \quad (2)$$

$$v_2 = k_2' N_{SS} n_1 = k_2 n_1$$

$$H_2O_{ads} + SS^- \xrightarrow{k_3'} H_{ads} + OH^- + SS^0 \quad (3)$$

$$v_3 = k_3'\Gamma_{H_2O}n_2 = k_3n_2$$

$$SS^- + h_{VB} \xrightarrow{k_4'} SS^0 \quad (4)$$

$$v_4 = k_4'p_sn_2 = k_4n_2$$

$$H_{ads} + H_{ads} \xrightarrow{k_5'} H_2 \quad (5)$$

$$v_5 = k_5'\Gamma_H^2$$

The electron-hole pairs generated under illumination (process 0) can recombine in the bulk or move to the surface. It is supposed that the flux of electrons that reach the surface (I_0) is directly proportional to the total incident photon flux (Φ_0), being the proportionality factor, K<1. K depends on different factors such as the nature and concentration of defects in the bulk of the semiconductor, the bending of the bands or the diffusion length of the electrons in the bulk.

$$I_0 = K\,\Phi_0 \quad (6)$$

Conduction band electrons can be transferred to solution (process 1) or to surface states (process 2). It is assumed that (under stationary conditions) only a minor fraction of the surface states are occupied by trapped electrons. The electrons trapped in surface states can react with adsorbed water (process 3) to produce adsorbed hydrogen. Photogenerated holes in the valence band can recombine with trapped electrons (process 4). Note that process 1 would correspond to the Volmer reaction step in the classical hydrogen evolution reaction (HER) mechanism. It is assumed that the second step of the HER is the Tafel reaction (process 5). However, the Heyrovsky electrodesorption step could also occur. In fact, both Tafel and Heyrovsky steps have been reported for the HER on metal oxide electrodes.[32-34]

In the following we hypothesize that process 3 is unlikely, and that the main pathway for water reduction is electron transfer from the conduction band (see section 4). Moreover, it is assumed that the value of Γ_{H_2O} is high and constant. Process 5 is assumed to be fast and thus process 1 is considered to be the rate determining step of the HER. The rate of reactions 0-5 (v_i) are expressed in $cm^{-2}\ s^{-1}$ and the rate constants k_1, k_2, k_3 and k_4 are given in s^{-1}.

The time-dependent concentrations of free minority carriers at the surface (n_1) and of minority carriers trapped at surface states (n_2) are defined by kinetic differential equations:

$$\frac{dn_1}{dt} = I_0 - k_1 n_1 - k_2 n_1 \quad (7)$$

$$\frac{dn_2}{dt} = k_2 n_1 - k_4 n_2 \quad (8)$$

This approach has been used in previous works[28,29,31] for either n-type or p-type semiconductor electrodes.

Three different capacitances in the SEI can be distinguished: the Helmholtz double layer capacitance (C_H), the space charge region capacitance (C_{SC}) and the capacitance of the surface states (C_{SS}). The importance of surface states in the photoresponse of semiconductor electrodes was extensively studied in the work of Li and Peter;[35] they determined that the presence of surface states induces a shift of the photocurrent onset toward positive potentials in the case of an n-type semiconductor. In the present work, the existence of surface states is considered to be described by a surface state capacitance charged through a resistor (R_{SS}), with a characteristic time constant for the trapping of minority carriers that can be expressed as $\tau_{SS} = R_{SS}\ C_{SS}$.

The drop of potential across the SEI is a function of these capacitances, as described in the classic theory of semiconductor electrochemistry[36,37]

$$j_{SS}R_{SS} + \phi_{SS} = \phi_{SC} = \phi - \phi_H \quad (9)$$

where j_{SS} is a capacitive current density related with the charge and discharge of the surface states.

On the other hand, the total electron flux across the interface can be expressed as the sum of a faradic component (superscript "F") and a capacitive component. Furthermore, the net flux of electrons (current) in the semiconductor side ($j_{electrode}$) of the interface must be equal to that in the electrolyte side ($j_{electrolyte}$). Similar theoretical treatments can be found in the literature.[28,38,39]

$$j_{electrolyte} = j_{electrode} \quad (10)$$

where:

$$j_{electrolyte} = j_H^F + C_H \frac{d\phi_H}{dt} \quad (11)$$

$$j_{electrode} = j_{SC}^F + C_{SC} \frac{d\phi_{SC}}{dt} + C_{SS} \frac{d\phi_{SS}}{dt} \quad (12)$$

$$j_H^F/e = -k_1 n_1 \quad (13)$$

$$j_{SC}^F/e = -I_0 + k_4 n_2 \quad (14)$$

Some assumptions or approximations are considered in the following discussion. First, the flux of electrons toward the surface (I_0) may be assumed as independent of the applied potential as long as the penetration depth of the light is smaller than the width of the depletion region or if the depletion region is not significantly affected by the applied potential.

Traditionally, the electric double layer in the SEI has been modeled as a combination of ideal capacitors. However, in real systems different non-idealities (porosity, surface roughness, chemical inhomogeneities, etc.) at the surface can produce frequency dispersion because of a non uniform distribution of the current density. The most frequently employed approximation in EIS to represent the deviation from purely capacitive behaviour at both the semiconductor side and the electrolyte side of the SEI is the introduction of a Constant Phase Element (CPE).[40–43] In this work, the electrical Helmholtz double layer is modeled as a CPE[44]:

$$Z_H = \frac{1}{R_H(i\omega)^{\psi}} = \frac{1}{R_H\omega^{\psi}}\left(\cos\frac{\psi\pi}{2} - i\,\mathrm{sen}\frac{\psi\pi}{2}\right) \quad (15)$$

instead of using the expression for a pure capacitance typical of an ideally polarizable electrode $Z_H = 1/(C_H\, i\omega)$. In equation 15, R_H is a constant and $0 < \psi < 1$ (where $\psi = 1$ corresponds to an ideal capacitor). As a result, the corresponding admittance can be expressed as:

$$Y_H = R_H\omega^{\psi}(Q+Pi) \quad (16)$$

where $Q = \cos(\psi\pi/2)$ and $P = \mathrm{sen}(\psi\pi/2)$.

The potential modulation is supposed to affect the band bending and, consequently, the concentration of majority carriers at the surface (p_S), which influences in turn the rate constant, k_4, as defined in the following equation:

$$k_4 = k_4'\, p_s = k_4^0\ \exp\left(\frac{\eta e\phi_{SC}}{kT}\right) \quad (17)$$

k_4^0 is the rate constant when $\phi_{SC} = 0$ (when the bands are flat) and η is an ideality factor.

The modulation of the potential across de Helmholtz layer will modify the activation energy and thus affect the rate constant k_1. Kühne et al[45] proposed the Tafel equation to describe the relationship between the interfacial charge transfer constant and the potential drop across the Helmholtz layer for p-InP. Analogously, here k_1 can be expressed as:

$$k_1 = k_1^0 \exp\left(\frac{-\alpha_c e \phi_H}{kT}\right) \quad (18)$$

Finally, we consider that the photoelectrochemical water reduction is not limited by mass transfer, and that the determining step is a charge transfer step.

The electrochemical impedance spectroscopy technique consists in the application of an ac perturbation to the potential dc signal, producing in turn a perturbation in the variables involved in the SEI. Frequently, a sinusoidal potential perturbation is applied to the electrode with a frequency $f = \omega/2\pi$:

$$\tilde{U} = |U| \exp(i\omega t) \quad (19)$$

Where $|U|$ is the amplitude of the perturbation and ω its angular frequency in rad s^{-1}. The ac component of the pertinent variables will be marked with a tilde ($\tilde{U}$, $\tilde{j}$, etc.). The admittance is defined as the ratio of the modulated current density and the modulated applied potential. Thus, the electrochemical impedance, $Z(\omega)$, the inverse of the admittance, $Y(\omega)$, will be given by:

$$Z(\omega) = \frac{1}{Y(\omega)} = \frac{\tilde{\phi}}{\tilde{j}} \quad (20)$$

The time-dependent expressions for the ac variables ($\tilde{k}_1$,$\tilde{k}_4$, $\tilde{\phi}_H$, $\tilde{\phi}_{SC}$, etc.) as well as the derivation of the equations for $\tilde{j}/\tilde{\phi}$ are given in the SI. They give rise to a general expression for the impedance as a function of the applied frequency:

$$Z(\omega) = R_s + \frac{\frac{i\omega A_1}{k_4 + i\omega} + \frac{i\omega A_2(k_2 + k_4 + i\omega)}{(k_1 + k_2 + i\omega)(k_4 + i\omega)} + i\omega\left(C_{sc} + \frac{C_{ss}}{1+i\omega\tau_{ss}}\right) + R_H\omega^{\psi}(Q+Pi)}{\left[R_H\omega^{\psi}(Q+Pi) + \frac{A_2(k_2 + i\omega)}{(k_1 + k_2 + i\omega)}\right]\left(\frac{i\omega A_1}{k_4 + i\omega} + i\omega\left(C_{sc} + \frac{C_{ss}}{1 + i\omega\tau_{ss}}\right)\right)} \quad (21)$$

where:

$$A_1 = \frac{k_2}{k_1+k_2}\ \frac{I_0\eta e^2}{kT} \quad (22)$$

$$A_2 = \frac{k_1}{k_1+k_2}\ \frac{I_0\alpha_c e^2}{kT} \quad (23)$$

2.2. Simulation of the impedance function

Theoretical simulations of the electrochemical impedance can be performed on the basis of equation 21. Taking into account the large number of parameters considered in the model, many possibilities for the impedance response can be conceived. Consequently, EIS plots may display a wide variety of shapes, depending on the relative values of the different parameters. A complete analysis of the different cases is beyond the scope of this work. The analysis will focus on the conditions under which the general expression of $Z(\omega)$ results in two semicircles, one at high frequencies (first semicircle) and the other at low frequencies (second semicircle). At high frequencies, the value of the rate constants can be neglected with respect to $i\omega$ in equation 21. The resulting expression for the first semicircle would be:

$$Z_{first}(\omega) = R_s + \frac{A_1+A_2+ i\omega\left(C_{sc} + \frac{C_{ss}}{1+i\omega\tau_{ss}}\right) + R_H\omega^{\psi}(P + Qi)}{(R_H\omega^{\psi}(P + Qi) + A_2)\left(A_1 + i\omega\left(C_{sc} + \frac{C_{ss}}{1 + i\omega\tau_{ss}}\right)\right)} \quad (24)$$

An expression for the intercept of the semicircle with the x-axis of the Nyquist plot (Z_{cross}) can be obtained from the low frequency limit ($\omega \rightarrow 0$) of equation 24:

$$Z_{cross} = R_s + \frac{A_1+A_2}{A_1\,A_2} = R_s + \frac{\frac{k_2}{k_1}+\frac{B}{A}}{B\,\frac{k_2}{(k_1+k_2)}}\frac{1}{eI_0} = R_s + \frac{\frac{k_2}{k_1}+\frac{B}{A}}{K\,B\,\frac{k_2}{(k_1+k_2)}}\frac{1}{e\Phi_0} \qquad (25)$$

The frequency at which the imaginary part of the impedance is maximum (ω_{max}) can also be determined as the time derivative of the imaginary part of equation 24 (assuming that $1 >> i\omega\tau_{SS}$). The following equation is obtained:

$$\omega_{max} = \frac{A_1}{C_{SC}+C_{SS}} = \frac{A\,\frac{k_2}{k_1+k_2}}{C_{SC}+C_{SS}}\,eI_0 = \frac{K\,A\,\frac{k_2}{k_1+k_2}}{C_{SC}+C_{SS}}\,e\Phi_0 \qquad (26)$$

In the region of the second semicircle, the terms related with the charge/discharge of both the surface states and the space charge layer (capacitive contributions, except that related with the CPE) can be neglected:

$$Z_{second}(\omega) = R_s + \frac{\frac{i\omega A_1}{k_4+i\omega} + \frac{i\omega A_2(k_2+k_4+i\omega)}{(k_1+k_2+i\omega)(k_4+i\omega)} + R_H\omega^{\psi}(P+Qi)}{\left[R_H\omega^{\psi}(P+Qi) + \frac{A_2(k_2+i\omega)}{(k_1+k_2+i\omega)}\right]\left(\frac{i\omega A_1}{k_4+i\omega}\right)} \qquad (27)$$

In the results and discussion section, the effect of applied potential and light intensity on the experimental behaviour of the $CaFe_2O_4$/FTO photoelectrode will be analyzed. Therefore, this section will illustrate changes in the electrochemical impedance response as a result of variations of either E or I_0.

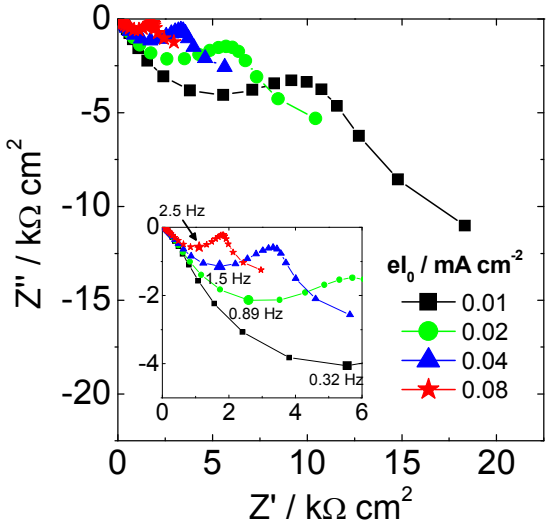

Figure 2. Nyquist plots calculated according to the theoretical model (equation 21) with $R_H = 2 \cdot 10^{-4}$ F cm^{-2} s$^{\psi-1}$, $\psi = 0.5$, $C_{SC} = 1.5 \cdot 10^{-5}$ F cm^{-2}, $C_{SS} = 6 \cdot 10^{-5}$ F cm^{-2}, $\tau_{SS} = 10^{-4}$ s^{-1}, $k_1 = 1.7 \cdot 10^{-2}$ s^{-1}, $k_2 = 1.7 \cdot 10^{-2}$ s^{-1}, $k_4 = 3 \cdot 10^{-2}$ s^{-1}, $R_S = 65$ Ω, $\alpha_C = 0.5$, $\eta = 1$ for eI_0 values ranging from 0.01 to 0.08 mA cm^{-2}.

First, the effect of I_0 on the EIS response is analysed on the basis of figure 2. Two semicircles are consistently observed in the Nyquist representation for the values chosen for the different parameters. As expected, the real and imaginary parts of the impedance increase with decreasing I_0. An analysis of the first semicircle on the basis of equations 25 and 26 reveals that, as long as the rate constants and K are not affected by the light intensity, Z_{cross} should be proportional to $1/I_0$ and ω_{max} should be proportional to I_0.

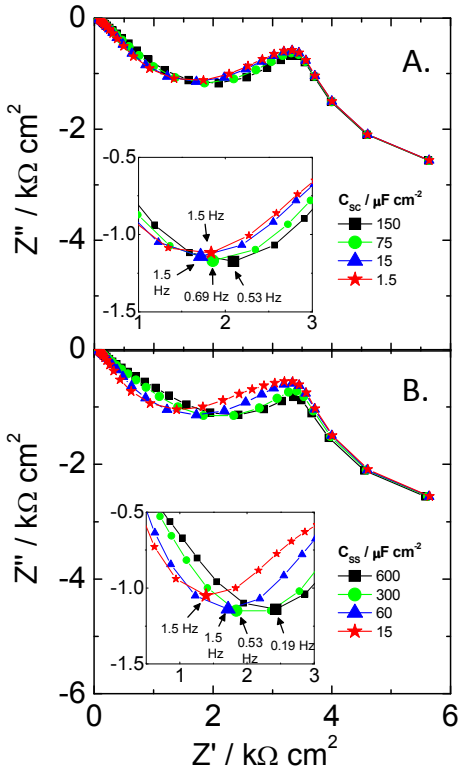

Figure 3. Nyquist plots built according to the theoretical model (equation 21) with $eI_0 = 0.04$ mA cm^{-2}, $R_H = 2 \cdot 10^{-4}$ F cm^{-2} s$^{\psi-1}$, $\psi = 0.5$, $\tau_{SS} = 10^{-4}$ s^{-1}, $k_1 = 1.7 \cdot 10^{-2}$ s^{-1}, $k_2 = 1.7 \cdot 10^{-2}$ s^{-1}, $k_4 = 3 \cdot 10^{-2}$ s^{-1}, $R_S = 65\ \Omega$, $\alpha_C = 1$, $\eta = 0.5$ (A) effect of C_{SC} ranging from $1.5 \cdot 10^{-4}$ to $1.5 \cdot 10^{-6}$ F cm^{-2} with $C_{SS} = 6 \cdot 10^{-5}$ F cm^{-2} and (B) effect of C_{SS} ranging from $6 \cdot 10^{-4}$ to $1.5 \cdot 10^{-5}$ F cm^{-2} with $C_{SC} = 1.5 \cdot 10^{-5}$ F cm^{-2}.

The influence of the magnitude of the depletion layer capacitance, C_{SC}, and the surface state capacitance, C_{SS}, on the impedance spectra is shown in figure 3. The semicircle at low frequencies is practically unaltered by changes of the capacitance values as it is predicted by equation 27. As the capacitance values change, the first semicircle is deformed in such manner that Z_{cross} remains constant, while ω_{max} is increasing as either C_{SC} or C_{SS} decrease. This is in agreement with model equations 25 and 26. For the lowest values of C_{SC} in figure 3A, the impedance response is virtually the same. This fact is explained on the basis of equation 21, in which C_{SC} and C_{SS} always appear combined as $C_{SC} + C_{SS}/(1+i\omega\tau_{SS})$. If the condition $C_{SC} << C_{SS}/(1+i\omega\tau_{SS})$ is fulfilled, C_{SC} becomes negligible and the EIS response

becomes independent of the depletion layer capacitance. In this case, Band Edge Pinning (BEP) would be precluded; and thus, the capacitance of the surface states together with the Helmholtz layer capacitance would govern the SEI.

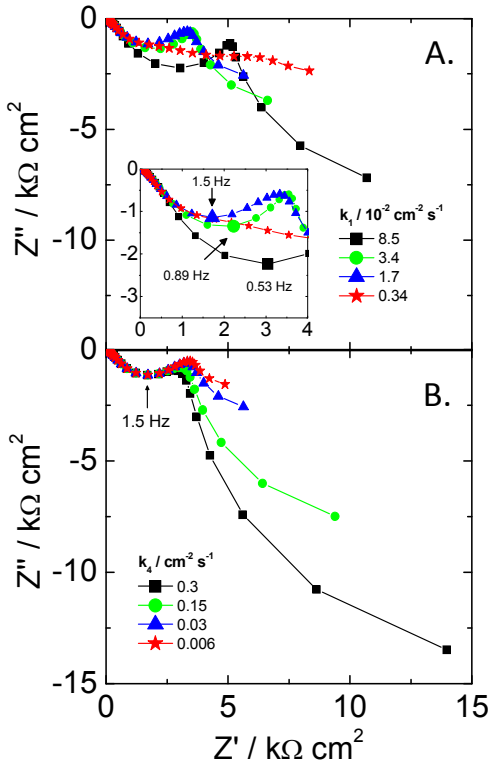

Figure 4. Nyquist plots calculated according to the theoretical model (equation 21) with $eI_0 = 0.04$ mA cm^{-2}, $R_H = 2 \cdot 10^{-4}$ F cm^{-2} s$^{\psi-1}$, $\psi = 0.5$, $C_{SC} = 1.5 \cdot 10^{-5}$ F cm^{-2}, $C_{SS} = 6 \cdot 10^{-5}$ F cm^{-2}, $\tau_{SS} = 10^{-4}$ s^{-1}, $k_2 = 1.7 \cdot 10^{-2}$ s^{-1}, $R_S = 65\ \Omega$, $\alpha_C = 1$, $\eta = 0.5$ (A) effect of k_1 ranging from $8.5 \cdot 10^{-2}$ to $3.4 \cdot 10^{-3}$ s^{-1} with $k_4 = 3 \cdot 10^{-2}$ s^{-1} and (B) effect of k_4 ranging from 0.3 to $6 \cdot 10^{-3}$ s^{-1} with $k_1 = 1.7 \cdot 10^{-2}$ s^{-1}.

In figure 4, the effect of the charge transfer constant (k_1) and the recombination constant (k_4) are investigated. Figure 4A illustrates that an increase in k_1 can either produce an increase or a decrease in the impedance depending on the frequency. The effect of this variable on both the first and second semicircles is significant. The variation of k_1 also affects the potential drop in the Helmholtz layer up to 10 Hz, as shown in the $|\tilde{\phi}_H/\tilde{\phi}|$ vs.

frequency plot (figure S1). The effect of k_1 on $|\tilde{\phi}_H/\tilde{\phi}|$ is especially intense at the lowest frequencies.

Additionally, Z_{cross} decreases with k_1 according to equation 25. Analysis of this equation unveils that Z_{cross} increases with k_1 when $k_1>k_2$ and decreases with k_1 when $k_2>k_1$. Importantly, the first condition implies the transfer of electrons from the conduction band to the electrolyte rather than their trapping at SS. The second condition represents the opposite situation. On the other hand, ω_{max} decreases when k_1 increases. When $k_1<<k_2$, ω_{max} is constant, according to equation 26. However, the effects on Z_{cross} and ω_{max} when $k_2>>k_1$ cannot be appreciated because when k_1 is sufficiently small ($k_1 = 3.4\cdot10^{-3}$ s^{-1} in figure 4A), the two semicircles converge to a curve without a well-defined shape.

Figure 4B displays the effect of k_4 on the impedance spectra. It is important to underline that the first semicircle is unaltered by the recombination rate constant, k_4, in agreement with equation 24. However, the effect in the second semicircle is obvious, producing an increase of the impedance with k_4.

In brief, in this section, it has been shown that the semicircle at low frequencies is mainly influenced by the kinetics of charge transfer and recombination processes, while the semicircle at high frequencies is not only strongly linked to the capacitances in the SEI, but also to the values of the kinetic constants k_1 and k_2.

3. EXPERIMENTAL SECTION

3.1. $CaFe_2O_4$ photoelectrode preparation. $CaFe_2O_4$ powder was prepared using a sol gel method described in the literature.[20,46] First, calcium (II) and iron (III) hydrated nitrates

were dissolved in water, and then, a solution of 5% of polyethylene glycol (PEG 6000) was added. The solvent was evaporated under stirring at 120 °C. The obtained gel was calcined at 450 °C for 2 h and then at 1050 °C for 2 h, originating a brown $CaFe_2O_4$ powder.

Electrode fabrication was performed using a platinum sheet as a substrate.[20] 50 mg of the powder was suspended in 100 μL of ethanol and was kept in an ultrasonic bath for 15 min. The suspension was dropped over the Pt sheet and the solvent was evaporated at room temperature. The deposited amount of $CaFe_2O_4$ was about 25 mg. Finally, the electrode was calcined at 1200 °C for 2 h and a dark brown 2-3 μm thick film of $CaFe_2O_4$ was finally obtained.

3.2. Physical characterization. X-ray diffraction (XRD) characterization was performed on a Seifert JSO-Debyeflex 2002 diffractometer using the Cu Kα line (λ= 1.5406 Å). A Shimadzu UV-2401PC spectrophotometer equipped with an integrating sphere coated with $BaSO_4$ was used to measure either UV-visible diffuse reflectance or absorbance spectra.

3.3. Photoelectrochemical and EIS analysis. Photoelectrochemical measurements were performed using a three-electrode cell equipped with a fused silica window. In order to avoid the platinum response in the electrochemical analysis, the bare substrate and part of the deposit were isolated by covering them with epoxy resin (PoxiPol ®) and then with a Teflon film over the resin. The active working electrode area was of 0.2 cm^2. A platinum wire was used as a counter electrode and all the potentials are measured and referred to an Ag/AgCl/KCl(3 M) reference electrode. All the (photo)electrochemical measurements were carried out by using a NOVA potenciostat coupled with a frequency response analyzer. The impedance measurements were performed using a $10\sqrt{2}$ mV amplitude perturbation in the

range of frequencies from 10 kHz to 3 mHz. A solar simulator SUN 2000 (Abet Technologies) was employed as a light source, using c.a. 1 sun of power irradiance and incorporating neutral density filters to set the irradiance as required. The actual irradiance ranged from 5 to 93 $mW \cdot cm^{-2}$.

4. RESULTS AND DISCUSSION

In this section, the validity of the developed model with the approximations established in section 2 will be checked for a $CaFe_2O_4$ photoelectrode. First, a brief discussion on the physicochemical characterization of the material is given. Second, the electrochemical response in the dark and under illumination are analyzed. Then, photoelectrochemical impedance spectroscopy is presented and discussed under different conditions. Finally, the experimental EIS data will be fitted with the developed model. In such a way, the model will be able to provide valuable information on the parameters determining the behavior of the illuminated SEI.

The characterization of the powder calcined at 1050 °C was performed by XRD and UV-visible spectroscopy. The XRD pattern (figure 5A) shows well defined peaks assigned to orthorhombic $CaFe_2O_4$ (JCPDS card 00-032-0168). The UV-visible absorption spectrum (figure 5B) shows a defined absorption edge starting at 650 nm, demonstrating that the material is able to absorb light in a rather wide range of the visible spectrum. The Tauc plot for a direct optical transition (inset in figure 5B) reveals a band gap of 1.85 eV in agreement with the value given in a previous report.[46]

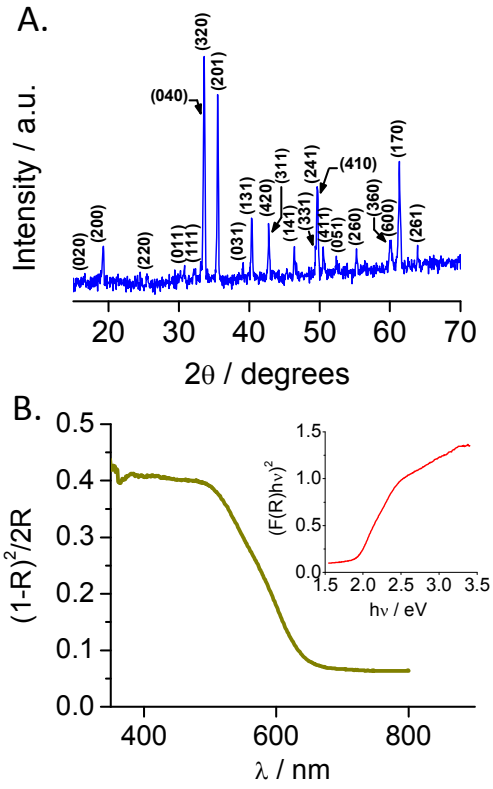

Figure 5. (A) X-ray diffraction pattern for the $CaFe_2O_4$ powder before being attached to a platinum substrate (B) UV-visible absorbance spectra calculated by means of the Kubelka-Munk function: $F(R) = (1-R)^2/(2R)$ from diffuse reflectance (R) measurements of a $CaFe_2O_4$ film on an FTO substrate and the corresponding Tauc plot considering a direct optical transition (inset).

The current-potential response in the dark for the thin film Pt/$CaFe_2O_4$ electrode in N_2-purged 0.1 M Na_2SO_4 is shown in figure 6A. In the positive potential region, a reversible capacitive process with larger currents appears, as expected for a p-type semiconductor electrode (accumulation region). The pair of small redox peaks located at 0.2-0.3 V is probably associated with the Pt substrate (see figure S2 in SI). At potentials positive to 0.5 V, irreversible currents attributed to the faradic reaction of water oxidation on the $CaFe_2O_4$ surface are observed.

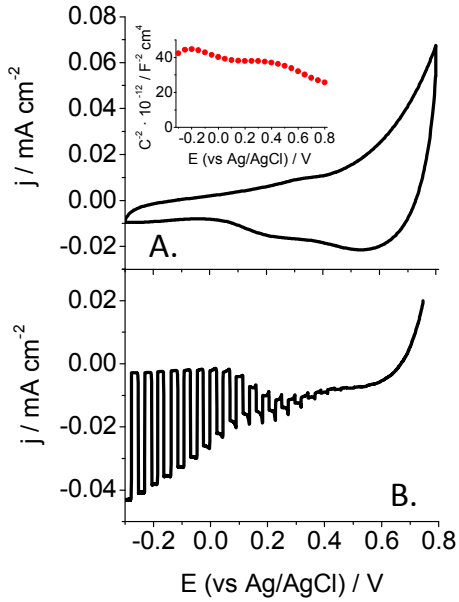

Figure 6. (A) Cyclic voltammogram in the dark in N_2-purged 0.1 M Na_2SO_4 (pH = 6) at 20 mV s^{-1} and Mott-Schottky representation calculated from the imaginary part of the impedance data at 1 kHz (inset) (B) Linear sweep voltammogram with transient solar simulator illumination of 93 mW cm^{-2}.

The current-potential curve under chopped illuminations in figure 6B reveals cathodic photocurrents in a broad range of potentials, as expected by considering the p-type nature of the material. The onset of the photocurrent is located at about 0.60 V vs. Ag/AgCl (1.15 V vs. RHE) at pH 6 (although clearer photocurrent are observed only below 0.4 V). This value is more positive than that reported by Cao et al[21] for FTO/$CaFe_2O_4$ electrodes prepared by PLD. The fact that the photocurrent onset is located within the accumulation region appearing in the high potential range suggests that this region can be attributed to the filling/emptying of surface states rather than to hole accumulation in the valence band. The contribution of Pt is negligible, although it cannot be completely discarded (see SI, figure S2). The photocurrent response was also recorded at pHs 13 (figure S3 in SI). Higher photocurrents were found in alkaline medium, being the observed onset in agreement with

that given by Ida et al.[20] Furthermore, the shift in the photocurrent onset with pH follows a Nernstian behavior of 0.06 V per pH unit (from pH 6 to pH 13).

The capacitance of the electrode was measured at different potentials and the Mott-Schottky plot is presented in the inset of figure 6A. The capacitance is almost constant in the investigated potential window. When the electrode interface is mainly governed by BEP, the Mott-Schottky plot exhibits a linear region[47–50] (with a negative slope in the case of a p-type semiconductor). As such linear region is not clearly defined in the present case, it is deduced that a modification of the applied potential is not mainly reflected in a change in the potential drop through the space charge region. The independence of the capacitance with the potential in $CaFe_2O_4$ pellets was already observed by Matsumoto et al.[18] They suggested that FLP occurs in the SEI due to the presence of surface states in the $CaFe_2O_4$ electrode.

A determination of the band gap and the flat band potential enables to situate the energetic position of the conduction and valence band edges. Unfortunately, the available data does not allow the determination of the flat band potential accurately; however, the onset of photocurrent is usually close to the flat band potential value (1.15 V vs. RHE). Following this approach, the conduction band edge is roughly estimated to be at -0.7 V vs. RHE. This means a maximum overvoltage of -0.7 V for water photoreduction. Electrons trapped in surface states have lower energies and consequently, their transfer to the reactive H_2O species would be more difficult or even impeded if the required overpotential for hydrogen evolution is higher in absolute value than the difference between the potential of the surface states and the redox potential for the hydrogen couple in the electrolytic medium. In this respect, it is envisageable that the transfer of electrons from the $CaFe_2O_4$ photoelectrode to

water molecules is more probably performed from the conduction band than from surface states.

The experimental EIS data for the $CaFe_2O_4$ electrode was recorded by setting the light intensity and recording the impedance spectra at different potentials from 0.4 V to -0.3 V (shown in figure S4). The photoelectrochemical response in the dark and after transient illumination was recorded before and after the EIS experiments at every light intensity. Cyclic voltammograms in the dark were unchanged after the EIS experiments, although the magnitude of the photocurrent was somewhat different, especially at the highest light intensities (see figure S5). This behavior may be attributed to an incipient irreversible reduction of the material during long illumination times under bias potential.

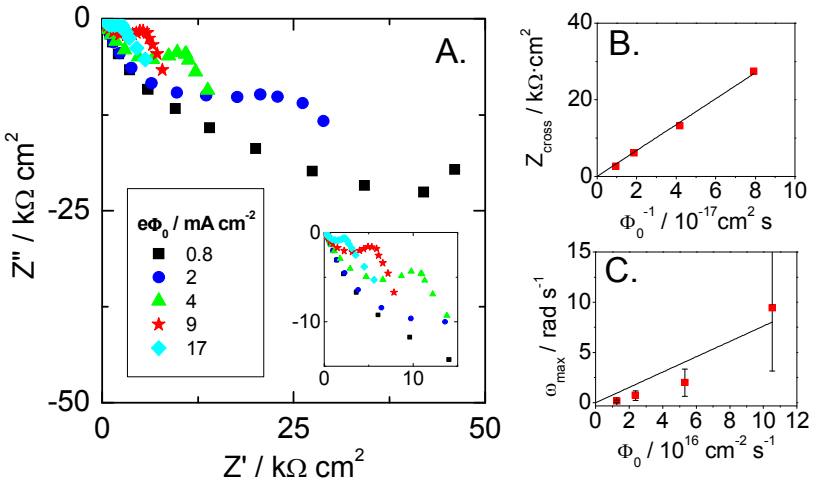

Figure 7. (A) Experimental Nyquist plots in N_2-purged 0.1 M Na_2SO_4 at a constant applied potential of 0 V vs. Ag/AgCl and different $e\Phi_0$ and (B) Z_{cross} and (C) ω_{max} for the first semicircle in the impedance curves represented in (A).

Photoelectrochemical impedance spectra for an applied potential of 0 V at different applied power irradiance are shown in figure 7A. The applied power irradiance ranges from 5 to 93

mW/cm^2. Based on the absorbance spectrum of the material, and the illumination source employed (solar simulator), for a quantum yield equal to one, the values of the power irradiance correspond to equivalent currents ($e\Phi_0$) ranging from 0.8 to 17 mA cm^{-2} (as estimated by considering step function absorbance at the wavelength corresponding to the band gap).[51] Visibly, a semicircle at high frequencies can be identified in the Nyquist plots. Moreover, a second region at lower frequencies is present. The assignment of this region to a transport process related with diffusion of the products and/or the charge carriers in the semiconductor[52–57] was discarded because diffusion processes emerge in EIS as straight lines with a slope of 45º (usually they are represented as Warburg elements in equivalent circuits). In this case, the angle is comprised between 40-60º and it changes with the applied potential. These facts suggest that the lower frequency part corresponds to a second semicircle of large radius.

In figure 7A, impedance decreases when $e\Phi_0$ increases for the all the studied potentials (see figure S4). A direct proportionality between the intercept of the semicircle with the x-axis (Z_{cross}) and the inverse of the irradiated light intensity is observed in figure 7B for an applied potential of 0 V, and also for -0.2 and -0.3 V, as shown in figure S6A. The experimental results clearly match the tendency predicted by the model (figure 2). In addition, the slope of the Z_{cross} vs. Φ_0^{-1} plot is similar from 0 to -0.3 V. According to equation 25, this indicates that the proportionality factor in equation 6, is indeed independent of irradiance. Also, it can be deduced that k_1 and k_2 must be almost independent of the applied irradiance (Z_{cross} is independent of k_4) and also of the applied potential from 0 to -0.3 V. Although, a priori, k_1 could be affected by the light intensity in an indirect way by alteration of the potential drop across the Helmholtz layer, this effect is

not present in this case, probably because of the low values of I_0 (see below). However, Ponomarev and Peter[31] found by IMPS that the recombination and transfer rate constants were affected by light intensity under strong light illumination.

Similar conclusions can be drawn from the plot of ω_{max} vs. Φ_0 shown in figure 7C (and figure S6B for potentials from 0 to -0.3 V) analyzed according to equation 26. However, a linear correlation of this parameter with Φ_0 is not so obvious probably because of the high error in the determination of ω_{max}.

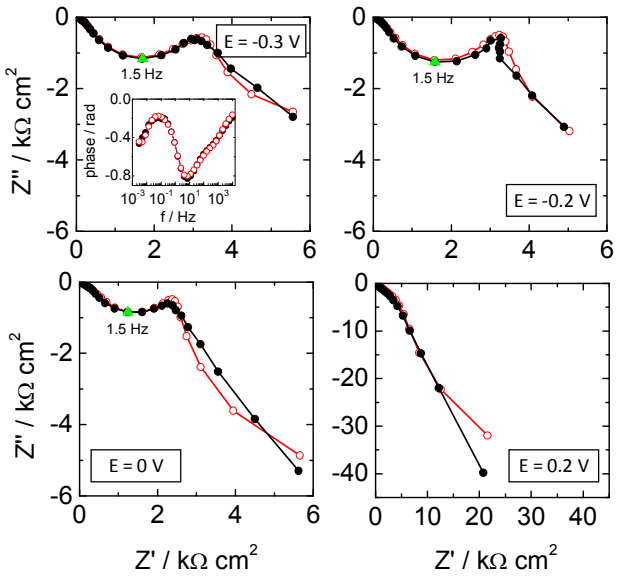

Figure 8. Nyquist plots using a light intensity of 93 mW cm^{-2} in N_2-purged 0.1 M Na_2SO_4 including experimental points (black solid symbols) and the simulated curves from the theoretical model (red open symbols) at different potentials referred to Ag/AgCl. The points corresponding to ω_{max} are marked in green. Inset represents experimental and simulated Bode plots for -0.3 V. Simulation parameters: $R_H = 2.3 \cdot 10^{-4}$ F cm^{-2} $s^{\psi-1}$, $\psi = 0.5$, $C_{SC} = 1.5 \cdot 10^{-5}$ F cm^{-2}, $\tau_{SS} = 1.7 \cdot 10^{-3}$ s, $R_S = 68$ Ω, $\alpha_C = 0.5$, $\eta = 1$, and I_0, C_{SS}, k_1, k_2 and k_4 are given in figure 9.

As mentioned earlier, working with a kinetic model instead of with an equivalent circuit is advantageous because all the parameters in the simulation possess a well-defined physical meaning. In figure 8 the most relevant results on the effect of the potential on the

impedance at a selected light intensity of 93 mW cm^{-2} are shown. It is important to highlight that the theoretical points fit very well the experimental data for every frequency in the whole range studied, which is clearly demonstrated in the Bode plot for -0.3 V shown in the inset of figure 8. In fact, there is a very good agreement between the calculated and the experimental Bode plots.

Admittedly, for the highest potentials the fit is worse. The reason may be the contribution of the dark component to the overall current, because the model is developed considering only the minority carriers generated under illumination. Consequently, its applicability is limited to the case when dark currents are negligible compared with the photocurrent.

The impedance is virtually potential-independent in the higher frequency range. This region is governed by parameters related with the capacitances of the double layer, revealing that some of these parameters such as R_H, C_{SC}, and τ_{SS}, can be considered as independent of applied potential.

For all the studied light intensities, impedance adopts comparable values at high reverse bias, and increase largely at potentials above 0 V, close to the photocurrent onset, as illustrated in figure S4. In fact, in figure 8, the impedance of the first semicircle reached similar values for applied potentials of -0.3, -0.2 and 0 V. Concretely, Z_{cross} and ω_{max} are very similar in the three cases (see also figure S6). According to the equations 25 and 26, the observed behavior suggests that I_0, k_1, k_2, C_{SC} and C_{SS} should change only slightly within this range of potential. On the other hand, figure 9A shows that the magnitude of I_0 does not change much upon varying the applied potential, which support the assumption that I_0 only depends on Φ_0, as previously discussed.

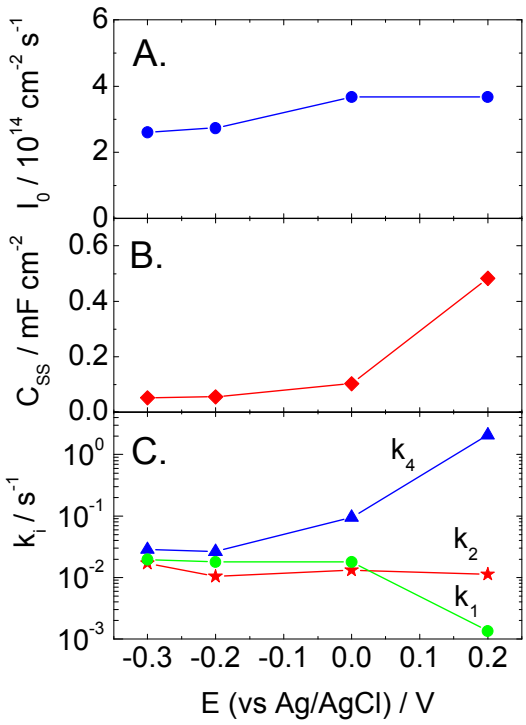

Figure 9. Parameters obtained by fitting the experimental impedance data in figure 8 to the theoretical model as a function of potential: (A) I_0 (B) C_{SS} and (C) k_1, k_2 and k_4.

As observed in figure 9B, C_{SS} increases with potential, especially for the highest potential values. Previously, the capacitive currents (accumulation region) in the dark starting at 0 V (figure 6) were correlated with the filling/emptying of surface states located at energies within the band gap (close to the valence band edge). The increase in C_{SS} can be tentatively correlated with such voltammetric region.

The fitting parameters obtained from the experimental data also reveal that C_{SS} is larger than C_{SC} for all the studied potentials. Thus, the part of the applied potential that drops in the semiconductor side of the interface, produce the charge/discharge of surface states, rather than an alteration of the space charge region. This is in agreement with the observed C^{-2} vs. E behavior (inset, figure 6A).

Working with CPE elements does not allow for a direct obtainment of the C_H value. However, the "effective equivalent capacitance, $C_{H,eff}$" of the Helmholtz layer can be estimated[58] as $R_H(\omega_{max})^{\psi-1}$ and it has a value of $7.5 \cdot 10^{-5}$ F cm^{-2}. The value of ω_{max} has been taken from the first semicircle in the Nyquist plots. The fact that $C_{H,eff}$ reaches the same order of magnitude than C_{SS} (which is significantly larger than C_{SC}) implies that changes in the applied potential would also affect the Helmholtz layer potential drop. This is confirmed in figure S7.

Regarding the dependence of the kinetic constants with the applied potential, the behavior observed in figure 9C is the expected one: k_4 increases with potential, k_1 decreases with the applied potential and k_2 does not significantly depend on potential. An increase in k_4 of about two orders of magnitude in the whole range of potential (0.5 V) is deduced after fitting the experimental impedance data. However, according to equation 17, a change of eight orders of magnitude would be expected for pure BEP behavior. Figure S7 simulate $\left|\tilde{\phi}_H/\tilde{\phi}\right|$ vs. frequency from equation A16 using the fitting parameters at each potential (according to figures 8 and 9). An average $\left|\tilde{\phi}_H/\tilde{\phi}\right|$ value of 0.7-0.8 can be roughly estimated. About a fourth of the applied potential change is reflected in the potential drop in the space charge region, which is in agreement with an increase of k_4 of two orders of magnitude instead of eight when increasing the applied potential by 0.5 V. Similarly, the decrease of k_1 with potential is smaller than that expected from equation 18, which reflects the fact that the electrode is not under Fermi Level Pinning (FLP) either.

The maximum flux of photogenerated electrons (Φ_0) can be roughly estimated as $1.1 \cdot 10^{17}$ cm^{-2} s^{-1} (17 mA cm^{-2}).[51] Therefore, a large difference is observed between Φ_0 and the actual

electron flux toward the surface (I_0); the I_0/Φ_0 ratio attains an average value of $3 \cdot 10^{-3}$. This means that only 0.3 % of the photogenerated electrons reach the surface. As important conclusion, this reveals that the main path for the recombination of electrons and holes occurs in the bulk of the semiconductor. The thick nature of the electrode and especially the fact that the electrode does not follow a BEP behavior favors recombination in the bulk of the semiconductor and impede an effective collection of charge carriers at the surface. This suggests that the concentration of electrons trapped in surface states is low, which is confirmed by the absence of large spikes upon tuning the light on an off in the photocurrent transients of figure 6. In addition this indicates that band bending cannot be greatly enhanced by applying potentials negative to the flat band potential as in such a case a drastic increase in I_0 should be observed, which is not the case.

The ratio between $k_1/(k_1+k_2)$ provides information about the fraction of electrons that are transferred to solution and the fraction that recombines with holes at surface states. For the highest potential value, the majority of electrons recombine ($k_1/(k_1+k_2)<<1$), this is reflected by small spikes (due to the low value of I_0) when light is turned on in figure 6 at 0.2 V. For lower potentials, the ratio is estimated to be 0.5-0.6, which would be reflected in higher stationary photocurrent values (equation A3).

The excellent agreement at both qualitative and quantitative levels between experiments and simulations clearly indicates that the assumptions upon which the model is based are plausible. The most critical hypothesis is that direct CB electron transfer is the predominant pathway for water reduction. This is in accordance with the fact that an attempt to adjust the experimental EIS data to a model equivalent to that of Leng,[28] in which indirect electron transfer from surface states is considered, leads to inconsistencies in the fitting parameters.

5. CONCLUSIONS

In this work, a novel photoelectrochemical impedance model based on a kinetic mechanism has been developed and applied for the investigation of hydrogen generation at the SEI of the Pt/$CaFe_2O_4$ p-type metal oxide photoelectrode. The mechanism proposed in the model is fully consistent with the experimental data. The presence of surface states is considered but only as electron trapping and recombination centers, being the conduction band electrons those directly transferred to water molecules. The quantitative agreement between experimental and calculated impedance data demonstrated by a simultaneous fit of both Nyquist and Bode plots is remarkable. It is worth nothing that the fit has been achieved by using only parameters with a clear physical meaning. Interestingly, the fit of the experimental data to the model reveals that most of the photogenerated charge carriers recombine in the bulk of the semiconductor, and that only a minor portion (0.3%) of the photogenerated electrons reaches the electrode surface. The concentration of trapped electrons in surface states is low, which is reflected in the chopped light voltammogram by the absence of spikes in the light transients. The values of the different interfacial capacitances resulting from the model reveal that the behavior of the $CaFe_2O_4$ SEI does not follow either Fermi level pinning or band edge pinning in agreement with the experimental Mott-Schottky plot. Importantly, the model considers the variation of the rate constants with the applied potential and it is found that all of them follow the expected trend, with the studied potential ranges, which is a strong validation of the underlying hypothesis.

In a more general vein, this contribution illustrates how a physicochemical model can be used to fit the experimental behavior of a p-type electrode in the context of photoelectrochemical water splitting, providing critical information on the water

photoreduction mechanism. By identifying the main losses in performance, it should help develop strategies for the improvement of the photoelectrode.

ASSOCIATED CONTENT

Supporting Information.

Derivation of the EIS expression, effect of k_1 on $|\tilde{\phi}_H/\tilde{\phi}|$ vs. frequency plot, cyclic voltammograms in the dark for a $Pt/CaFe_2O_4$ electrode with and without insulate the free Pt surface, linear scan voltammograms with transient illumination at pH = 13 and 6, Nyquist plots at different light intensities and different potentials, linear scan voltammograms with transient illumination and cyclic voltammograms in the dark before and after the EIS experiments, Z_{cross} vs. Φ_0^{-1} and ω_{max} vs. Φ_0 plots at different potentials, $|\tilde{\phi}_H/\tilde{\phi}|$ as a function of the frequency for the different applied potentials.

This material is available free of charge via the Internet at http://pubs.acs.org.

AUTHOR INFORMATION

Corresponding Author

* E-mail: Roberto.Gomez@ua.es (R. G.).

Notes

The authors declare no competing financial interest.

ACKNOWLEDGMENT

The authors gratefully acknowledge the financial support of the Spanish Ministry of Economy and Competitiveness through projects MAT2012-37676 and MAT2015-71727-R both cofinanced by FEDER funds.

ABBREVIATIONS

α_C, Cathodic charge transfer coefficient; C_H, Helmholtz layer capacitance (F cm^{-2}); C_{SC}, Space charge layer capacitance (F cm^{-2}); C_{SS}, Surface state capacitance (F cm^{-2}); e, Elementary charge ($1.6 \cdot 10^{-19}$ C); E, Applied potential (V); ϕ, Total applied potential drop across the double layer (V); ϕ_H, Potential drop across the Helmholtz layer (V); ϕ_{SC}, Potential drop across the space charge layer (V); ϕ_{SS}, Potential drop related with surface states (V); Φ_0, Maximum flux of photogenerated electrons (cm^{-2} s^{-1}); Γ_{H_2O}, Surface density of adsorbed water molecules (cm^{-2}); N_{ss}, surface state density (cm^{-2}); η, Ideality factor; I_0, Flux of electrons toward the semiconductor surface (cm^{-2} s^{-1}); j, Current density (A cm^{-2}); j_{SC}^F, Faradic current density in the electrode side of the interface; j_H^F, Faradic current density in the electrolyte side of the interface; j_{SS}, Current density associated with the charging of the surface state capacitance (A cm^{-2}); k, Boltzmann constant ($1.38 \cdot 10^{23}$ J K^{-1}); k_i, Kinetic constants (s^{-1}); K, Proportionality factor, K<1 (dimensionless); n_1, Instantaneous density of free electrons at the surface (cm^{-2}); n_2, Instantaneous density of electrons trapped in surface states (cm^{-2}); p_S, Hole density at the semiconductor surface (cm^{-2}); R_H, Parameter of the CPE model related with the charge/discharge of the Helmholtz layer (F cm^{-2} $s^{\psi-1}$); R_s, Electrolytic solution resistance (Ω); R_{SS}, Surface states resistance (Ω cm^2); SS, Surface states; T, Absolute temperature (K); t, Time (s); τ_{SS}, Time constant for the

charge/discharge of surface states (s); ω, Angular frequency (rad s^{-1}); ω_{max}, Frequency at the maximum of the imaginary part of the impedance of the high frequency semicircle in the Nyquist plot (rad s^{-1}); ψ, Parameter of CPE model (dimensionless).

REFERENCES

(1) Monllor-Satoca, D.; Lana-Villarreal, T.; Gómez, R. Effect of Surface Fluorination on the Electrochemical and Photoelectrocatalytic Properties of Nanoporous Titanium Dioxide Electrodes. *Langmuir* **2011**, *27*, 15312–15321.

(2) Jankulovska, M.; Barceló, I.; Lana-Villarreal, T.; Gómez, R. Improving the Photoelectrochemical Response of TiO_2 Nanotubes upon Decoration with Quantum-Sized Anatase Nanowires. *J. Phys. Chem. C* **2013**, *117*, 4024–4031.

(3) Lee, D. H.; Song, D.; Kang, Y. S.; Park, W. Il. Three-Dimensional Monolayer Graphene and TiO_2 Hybrid Architectures for High-Efficiency Electrochemical Photovoltaic Cells. *J. Phys. Chem. C* **2015**, *119*, 6880–6885.

(4) Hu, Y.; Bora, D. K.; Boudoire, F.; Häussler, F.; Graetzel, M.; Constable, E. C.; Braun, A. A Dip Coating Process for Large Area Silicon-Doped High Performance Hematite Photoanodes. *J. Renew. Sustain. Energy* **2013**, *5*, 043109.

(5) Tallarida, M.; Das, C.; Cibrev, D.; Kukli, K.; Tamm, A.; Ritala, M.; Lana-Villarreal, T.; Gómez, R.; Leskelä, M.; Schmeisser, D. Modification of Hematite Electronic Properties with Trimethyl Aluminum to Enhance the Efficiency of Photoelectrodes. *J. Phys. Chem. Lett.* **2014**, *5*, 3582–3587.

(6) Fujimoto, I.; Wang, N.; Saito, R.; Miseki, Y.; Gunji, T.; Sayama, K. $WO_3/BiVO_4$

Composite Photoelectrode Prepared by Improved Auto-Combustion Method for Highly Efficient Water Splitting. *Int. J. Hydrogen Energy* **2014**, *39*, 2454–2461.

(7) Zhang, L.; Lin, C. Y.; Valev, V. K.; Reisner, E.; Steiner, U.; Baumberg, J. J. Plasmonic Enhancement in $BiVO_4$ Photonic Crystals for Efficient Water Splitting. *Small* **2014**, *10*, 3970–3978.

(8) Quiñonero, J.; Lana–Villarreal, T.; Gómez, R. Improving the Photoactivity of Bismuth Vanadate Thin Film Photoanodes through Doping and Surface Modification Strategies. *Appl. Catal. B Environ.* **2016**, *194*, 141–149.

(9) Siripala, W.; Ivanovskaya, A.; Jaramillo, T. F.; Baeck, S. H.; McFarland, E. W. A Cu_2O/TiO_2 Heterojunction Thin Film Cathode for Photoelectrocatalysis. *Sol. Energy Mater. Sol. Cells* **2003**, *77*, 229–237.

(10) Paracchino, A.; Laporte, V.; Sivula, K.; Grätzel, M.; Thimsen, E. Highly Active Oxide Photocathode for Photoelectrochemical Water Reduction. *Nat. Mater.* **2011**, *10*, 456–461.

(11) Hsu, Y.-K.; Yu, C.-H.; Chen, Y.-C.; Lin, Y.-G. Synthesis of Novel Cu_2O Micro/nanostructural Photocathode for Solar Water Splitting. *Electrochim. Acta* **2013**, *105*, 62–68.

(12) Morales-Guio, C. G.; Liardet, L.; Mayer, M. T.; Tilley, S. D.; Grätzel, M.; Hu, X. Photoelectrochemical Hydrogen Production in Alkaline Solutions Using Cu_2O Coated with Earth-Abundant Hydrogen Evolution Catalysts. *Angew. Chemie Int. Ed.* **2015**, *54*, 664–667.

(13) Celorrio, V.; Bradley, K.; Weber, O. J.; Hall, S. R.; Fermín, D. J. Photoelectrochemical Properties of $LaFeO_3$ Nanoparticles. *ChemElectroChem* **2014**, *1*, 1667-1671.

(14) Yu, Q.; Meng, X.; Wang, T.; Li, P.; Liu, L.; Chang, K.; Liu, G.; Ye, J. Highly Durable p-$LaFeO_3$/n-Fe_2O_3 Photocell for Effective Water Splitting under Visible Light. *Chem. Commun.* **2015**, *51*, 3630–3633.

(15) Díaz-García, A. K.; Lana-Villarreal, T.; Gómez, R. Sol–gel Copper Chromium Delafossite Thin Films as Stable Oxide Photocathodes for Water Splitting. *J. Mater. Chem. A* **2015**, *3*, 19683–19687.

(16) Prévot, M. S.; Guijarro, N.; Sivula, K. Enhancing the Performance of a Robust Sol-Gel-Processed p-Type Delafossite $CuFeO_2$ Photocathode for Solar Water Reduction. *ChemSusChem* **2015**, *8*, 1359–1367.

(17) Joshi, U. A.; Palasyuk, A. M.; Maggard, P. A. Photoelectrochemical Investigation and Electronic Structure of a p-Type $CuNbO_3$ Photocathode. *J. Phys. Chem. C* **2011**, *115*, 13534–13539.

(18) Matsumoto, Y.; Omae, M.; Sugiyama, K.; Sato, E. New Photocathode Materlals for Hydrogen Evolution: $CaFe_2O_4$ and $Sr_7Fe_{10}O_{22}$. *J. Phys. Chem.* **1987**, *91*, 577–581.

(19) Company, P. Photoelectrochemical Properties of $LuRhO_3$. *Surf. Sci.* **1980**, *101*, 205–213.

(20) Ida, S.; Yamada, K.; Matsunaga, T.; Hagiwara, H.; Matsumoto, Y.; Ishihara, T. Preparation of p-Type $CaFe_2O_4$ Photocathodes for Producing Hydrogen from Water.

J. Am. Chem. Soc. **2010**, *132*, 17343–17345.

(21) Cao, J.; Kako, T.; Li, P.; Ouyang, S.; Ye, J. Fabrication of p-Type $CaFe_2O_4$ Nanofilms for Photoelectrochemical Hydrogen Generation. *Electrochem. commun.* **2011**, *13*, 275–278.

(22) Lopes, T.; Andrade, L.; Ribeiro, H. A.; Mendes, A. Characterization of Photoelectrochemical Cells for Water Splitting by Electrochemical Impedance Spectroscopy. *Int. J. Hydrogen Energy* **2010**, *35*, 11601–11608.

(23) Shimizu, K.; Lasia, A. Electrochemical Impedance Study of the Hematite/Water Interface. *Langmuir* **2012**, *28*, 7914–7920.

(24) Klahr, B.; Gimenez, S.; Fabregat-Santiago, F.; Hamann, T.; Bisquert, J. Water Oxidation at Hematite Photoelectrodes: The Role of Surface States. *J. Am. Chem. Soc.* **2012**, *134*, 4294–4302.

(25) Klahr, B.; Gimenez, S.; Fabregat-Santiago, F.; Bisquert, J.; Hamann, T. W. Electrochemical and Photoelectrochemical Investigation of Water Oxidation with Hematite Electrodes. *Energy Environ. Sci.* **2012**, *5*, 7626–7636.

(26) Gimenez, S.; Dunn, H. K.; Rodenas, P.; Fabregat-Santiago, F.; Miralles, S. G.; Barea, E. M.; Trevisan, R.; Guerrero, A.; Bisquert, J. Carrier Density and Interfacial Kinetics of Mesoporous TiO_2 in Aqueous Electrolyte Determined by Impedance Spectroscopy. *J. Electroanal. Chem.* **2012**, *668*, 119–125.

(27) Wang, Y.; Cui, X.; Zhang, Y.; Gao, X.; Sun, Y. Preparation of Cauliflower-like ZnO Films by Chemical Bath Deposition: Photovoltaic Performance and Equivalent

Circuit of Dye-Sensitized Solar Cells. *J. Mater. Sci. Technol.* **2013**, *29*, 123–127.

(28) Leng, W. H.; Zhang, Z.; Zhang, J. Q.; Cao, C. N. Investigation of the Kinetics of a TiO_2 Photoelectrocatalytic Reaction Involving Charge Transfer and Recombination through Surface States by Electrochemical Impedance Spectroscopy. *J. Phys. Chem. B* **2005**, *109*, 15008–15023.

(29) Peter, L. M.; Ponomarev, E. A.; Fermín, D. J. Intensity-Modulated Photocurrent Spectroscopy: Reconciliation of Phenomenological Analysis with Multistep Electron Transfer Mechanisms. *J. Electroanal. Chem.* **1997**, *427*, 79–96.

(30) Liu, H.; Li, X. Z.; Leng, Y. J.; Li, W. Z. An Alternative Approach to Ascertain the Rate-Determining Steps of TiO_2 Photoelectrocatalytic Reaction by Electrochemical Impedance Spectroscopy. *J. Phys. Chem. B* **2003**, *107*, 8988–8996.

(31) Ponomarev, E. A.; Peter, L. M. A Comparison of Intensity Modulated Photocurrent Spectroscopy and Photoelectrochemical Impedance Spectroscopy in a Study of Photoelectrochemical Hydrogen Evolution at p-InP. *J. Electroanal. Chem.* **1995**, *397*, 45–52.

(32) Losiewicz, B.; Budniok, A.; Rowinski, E.; Lagiewka, E.; Lasia, A. Effect of Heat-Treatment on the Mechanism and Kinetics of the Hydrogen Evolution Reaction on Ni-P+TiO_2+Ti electrodes. *J. Appl. Electrochem.* **2004**, *34*, 507–516.

(33) Lačnjevac, U. Č.; Jović, B. M.; Jović, V. D.; Krstajić, N. V. Determination of Kinetic Parameters for the Hydrogen Evolution Reaction on the Electrodeposited Ni–MoO_2 Composite Coating in Alkaline Solution. *J. Electroanal. Chem.* **2012**, *677-*

680, 31–40.

(34) Aruna, K. K.; Manoharan, R. Electrochemical Hydrogen Evolution Catalyzed by $SrMoO_4$ Spindle Particles in Acid Water. *Int. J. Hydrogen Energy* **2013**, *38*, 12695–12703.

(35) Li, J.; Peter, L. Surface Recombination at Semiconductors Electrodes. Part III. Steady-State and Intensity Modulated Photocurrent Response. *J. Electroanal. Chem.* **1985**, *193*, 27–47.

(36) Pleskov, Y. V.; Gurevich, Y. Y. *Semiconductor Photoelectrochemistry*; Consultants Bureau: New York, 1986.

(37) Bard, A. J.; Bocarsly, A. B.; Fan, F. F.; Walton, E. G.; Wrighton, M. S. The Concept of Fermi Level Pinning at Semiconductor/Liquid Junctions. Consequences for Energy Conversion Efficiency and Selection of Useful Solution Redox Couples in Solar Devices. *J. Am. Chem. Soc.* **1980**, *102*, 3671–3677.

(38) Vanmaekelbergh, D. Direct and Surface State Mediated Electron Transfer at Semiconductor/electrolyte junctions—I. A Comparison of Steady-State Results. *Electrochim. Acta* **1997**, *42*, 1121–1134.

(39) Hens, Z. The Electrochemical Impedance of One-Equivalent Electrode Processes at Dark Semiconductor/Redox Electrodes Involving Charge Transfer through Surface States. 1. Theory. *J. Phys. Chem. B* **1999**, *103*, 122–129.

(40) Pleskov, Y. V.; Elkin, V. V.; Abaturov, M. A.; Krotova, M. D.; Mishuk, V. Y.; Varnun, V. P.; Teremetskaya, I. G. Synthetic Semiconductor Diamond Electrodes:

Elucidation of the Equivalent Circuit for the Case of Frequency-Dependent Impedance. *J. Electroanal. Chem.* **1996**, *413*, 105–110.

(41) Spagnol, V.; Sutter, E.; Debiemme-Chouvy, C.; Cachet, H.; Baroux, B. EIS Study of Photo-Induced Modifications of Nano-Columnar TiO_2 Films. *Electrochim. Acta* **2009**, *54*, 1228–1232.

(42) Hirschorn, B.; Orazem, M. E.; Tribollet, B.; Vivier, V.; Frateur, I.; Musiani, M. Constant-Phase-Element Behavior Caused by Resistivity Distributions in Films: II. Applications. *J. Electrochem. Soc.* **2010**, *157*, C458–C463.

(43) Lasia, A. *Electrochemical Impedance Spectroscopy and Its Applications*; Springer Science+Business Media: New York, 2014.

(44) Rammelt, U.; Reinhard, G. On the Applicability of a Constant Phase Element (CPE) to the Estimation of Roughness of Solid Metal Electrodes. *Electrochim. Acta* **1990**, *35*, 1045–1049.

(45) Kühne, H.-M.; Schefold, J. Tafel Plots from Illuminated Photoelectrodes. A New Insight Into Charge Transfer Mechanism. *J. Electrochem. Soc.* **1990**, *137*, 568–575.

(46) Liu, Z.; Zhao, Z. G.; Miyauchi, M. Efficient Visible Light Active $CaFe_2O_4/WO_3$ Based Composite Photocatalysts: Effect of Interfacial Modification. *J. Phys. Chem. C* **2009**, *113*, 17132–17137.

(47) Khan, S. U. M.; Akikusa, J. Photoelectrochemical Splitting of Water at Nanocrystalline n-Fe_2O_3 Thin-Film Electrodes. *J. Phys. Chem. B,* **1999**, *103*, 7184–7189.

(48) Paracchino, A.; Mathews, N.; Hisatomi, T.; Stefik, M.; Tilley, S. D.; Grätzel, M. Ultrathin Films on Copper(I) Oxide Water Splitting Photocathodes: A Study on Performance and Stability. *Energy Environ. Sci.* **2012**, *5*, 8673-8681.

(49) Gurudayal, G.; Chiam, S. Y.; Kumar, M. H.; Bassi, P. S.; Seng, H. L.; Barber, J.; Wong, L. H. Improving the Efficiency of Hematite Nanorods for Photoelectrochemical Water Splitting by Doping with Manganese. *ACS Appl. Mater. Interfaces* **2014**, *6*, 5852–5859.

(50) Digdaya, I. A.; Han, L.; Thom, W. F. B.; Zeman, M, Dam, B.; Smets, A. H. M.; Smith, W. A. Extracting Large Photovoltages from a-SiC Photocathodes with an Amorphous TiO_2 Front Surface Field Layer for Solar Hydrogen Evolution. *Energy Environ. Sci*. **2015**, *8*, 1585-1593.

(51) Smestad, G. P.; Krebs, F. C.; Lampert, C. M.; Granqvist, C. G.; Chopra, K. L.; Mathew, X.; Takakura, H. Reporting Solar Cell Efficiencies in Solar Energy Materials and Solar Cells. *Sol. Energy Mater. Sol. Cells* **2008**, *92*, 371–373.

(52) Hens, Z.; Gomes, W. P. On the Diffusion Impedance at Semiconductor Electrodes. *J. Phys. Chem. B* **1997**, *101*, 5814–5821.

(53) Bisquert, J.; Garcia-Belmonte, G.; Bueno, P.; Longo, E.; Bulhões, L. O. Impedance of Constant Phase Element (CPE)-Blocked Diffusion in Film Electrodes. *J. Electroanal. Chem.* **1998**, *452*, 229–234.

(54) Bisquert, J.; Garcia-Belmonte, G.; Fabregat-Santiago, F.; Bueno, P. R. Theoretical Models for ac Impedance of Diffusion Layers Exhibiting Low Frequency

Dispersion. *J. Electroanal. Chem.* **1999**, *475*, 152-163.

(55) Bisquert, J.; Compte, A. Theory of the Electrochemical Impedance of Anomalous Diffusion. *J. Electroanal. Chem.* **2001**, *499*, 112–120.

(56) Arutyunyan, V. M.; Arakelyan, V. M.; Shakhnazaryan, G. E.; Stepanyan, G. M.; Turner, J. A.; Khaselev, O. Investigation of Ceramic Fe_2O_3 (Ta) Photoelectrodes for Photoelectrochemical Solar Cells. *Russ. J. Electrochem.* **2002**, *38*, 378–383.

(57) Aroutiounian, V. M.; Arakelyan, V. M.; Shahnazaryan, G. E.; Hovhannisyan, H. R.; Wang, H.; Turner, J. A. Photoelectrochemistry of Tin-Doped Iron Oxide Electrodes. *Sol. Energy* **2007**, *81*, 1369–1376.

(58) Hsu, C. H.; Mansfeld, F. Concerning the Conversion of the Constant Phase Element Parameter Y_0 into a Capacitance. *Corrosion*, **2001**, *57*, 747-748.

Insert Table of Contents Graphic and Synopsis Here